

## Research Article

# Parametric Study on the Seismic Response of Steel-Framed Buildings with Self-Centering Tension-Only Braces

Pei Chi ,<sup>1,2</sup> Wenlong Tian ,<sup>1</sup> Tong Guo ,<sup>2</sup> Dafu Cao ,<sup>1</sup> and Jun Dong ,<sup>3</sup>

<sup>1</sup>College of Civil Science and Engineering, Yangzhou University, Yangzhou 225009, China

<sup>2</sup>School of Civil Engineering, Southeast University, Nanjing 210096, China

<sup>3</sup>College of Civil Engineering, Nanjing Tech University, Nanjing 211816, China

Correspondence should be addressed to Pei Chi; chipei@yzu.edu.cn

Received 7 July 2019; Revised 3 August 2019; Accepted 6 August 2019; Published 25 August 2019

Academic Editor: Rosario Montuori

Copyright © 2019 Pei Chi et al. This is an open access article distributed under the Creative Commons Attribution License, which permits unrestricted use, distribution, and reproduction in any medium, provided the original work is properly cited.

Self-centering bracing systems, by which residual deformations of structures after earthquakes can be minimized, are considered effective solutions to achieve seismic resilience. In this paper, a parametric study on the seismic response of intermediate and high-rise steel-framed buildings with novel self-centering tension-only braces (SC-TOBs) is numerically conducted. Three key parameters, the stiffness degradation factor, the activation strain, and the initial axial stiffness of the SC-TOBs, are investigated to explore the design space for the SC-TOB frames (SC-TOBFs) because of their unique tunability compared with traditional bracing systems. Identical steel frames equipped with buckling restrained braces (BRBs) are also designed and examined for comparison purposes. The results indicate that increasing the stiffness degradation factor can improve the second stiffness of SC-TOBFs and successfully make the distribution of interstory drifts more uniform; an increase in the activation strain leads to a larger activation deformation of SC-TOBFs, but it has a very limited effect on the interstory drifts; increasing the initial axial stiffness appropriately is beneficial to reduce the interstory drifts of the low stories. The lateral behavior of SC-TOBFs is comparable to that of BRB frames when a lower activation strain and a higher initial axial stiffness are selected. Furthermore, when a higher stiffness degradation factor and a lower initial axial stiffness are selected simultaneously, the seismic action on SC-TOBFs can be effectively reduced, and a relatively uniform distribution over the building height can be obtained. The SC-TOBFs are considered to be a type of performance-tunable structure, and tuning can be achieved by varying a frame's adjustable parameters.

## 1. Introduction

Controlling inelastic ductility to soften the seismic response and to dissipate the hysteretic energy is a basic concept for the seismic design of structures. However, inelastic ductility can also result in the concentration of damage in local parts of a structure and produce residual deformations (e.g., [1–3]), leading to undesirable influences on the resulting structure in terms of prohibitive costs of rehabilitation for structural and nonstructural components, interruption of building function, and a high collapse risk due to the  $P$ -delta effects [4–8].

Braced frames are lateral resisting systems that have been commonly used in steel buildings for earthquake resistance. To reduce or eliminate residual deformations, Christopoulos et al. [9] proposed a self-centering energy dissipative (SCED)

brace, which provided a restoring force by pretensioned (PT) aramid fiber-reinforced polymer (AFRP) elements and energy dissipation through a friction mechanism. Quasistatic and dynamic tests demonstrated that the SCED brace had satisfactory recentering and energy dissipation capacities, and its bracing system could self-center within the target design drift. To confirm the seismic performance of the SCED braces within structures, Erochko et al. [7] carried out a shake table test on a 3-story steel frame braced with SCED braces and performed numerical simulations for comparison. To improve the recentering capability of self-centering braces (SCBs), the enhanced elongation telescoping SCED (T-SCED) brace and the dual-core SCB (DC-SCB), both of which incorporate multiple self-centering systems, were developed independently [10, 11]. A full-scale one-story one-bay steel frame with DC-SCBs was tested to examine its

seismic performance, and the results showed that the initial axial stiffness of the DC-SCB would decrease significantly from the influence of fabrication errors [12, 13].

Buckling restrained braces (BRBs), which have symmetric hysteretic behaviors and excellent energy dissipation capacity, have been widely used in recent years. However, this bracing system tends to induce large residual deformations after an earthquake [14, 15]. To address this drawback, Liu and Wu [16] proposed the self-centering BRB (SC-BRB) using PT steel strands to provide a restoring force. Chou et al. [17] proposed a dual-core self-centering sandwiched BRB (SC-SBRB) combining the self-centering property of a DC-SCB and the energy dissipation of a sandwiched BRB. Multiple cyclic tests demonstrated that the SC-SBRB exhibited appreciable self-centering, deformation, and energy dissipation capacities. Zhou et al. [18, 19] used basalt fiber-reinforced polymer for the PT tendons and developed a dual-tube SC-BRB, which exhibited a good flag-shaped hysteretic performance and self-centering capacity. Xie et al. [20] improved the dual-tube SC-BRB configuration by adding a rubber cushion so as to reduce the negative influence of the fabrication error. Other feasible solutions for braces to achieve self-centering, such as prepressed springs, and energy dissipation, such as magnetorheological fluid devices, can be found in the literature [21–23]. In addition, shape memory alloys (SMAs), characterized by superelasticity to recenter and dissipate energy on their own, have been employed to develop various types of SMA-based braces [24–26].

Unlike the abovementioned relatively rigid braces, tension-only braces (TOBs) are flexible bracing members, which can enable the full use of high-strength materials without buckling under compression, leading to a mitigated seismic response of the braced structures due to a prolonged fundamental period. Thus, TOBs have many applications in buildings in areas of low seismicity [27–29]. However, because of their severe pinched hysteresis and inferior energy dissipation capacity, TOBs are prohibited as the sole lateral resistant system in areas of high seismicity [30, 31]. Regardless of these drawbacks, a lot of efforts have been made to expand the application of TOBs. For example, Mousavi and Zahrai [32] proposed a preslacked cable brace (PSCB), and their numerical study indicated that PSCBs could eliminate the strength degradation of the braced nonductile frame. Thereafter, Mousavi and Zahrai [33] proposed a slack-free connection (SFC), by which the pinching of the TOBs could be completely avoided and energy dissipation capacity was thereby significantly improved. Zahrai et al. [34] proposed a hybrid TOB (HTOB), which has a stable hysteresis with tunable postyield stiffness. Mehrabi et al. [35] proposed a TOB system with a precompressed spring, which enables both diagonal bracings to be constantly in tension. Experimental and analytical investigations validated the enhanced lateral performance of the cable braced frames in terms of strength and ductility.

In light of these studies, to take advantage of the seismic resilience of SCBs and the seismic mitigation of TOBs, a novel self-centering TOB (SC-TOB) has been developed and numerically verified by Chi et al. [36, 37].

To further investigate how the SC-TOBs can be implemented in structures to improve seismic performance, a parametric study on the seismic response of 9- and 16-story steel-framed buildings, which can be considered typical of intermediate and high-rise buildings, with SC-TOBs is numerically conducted through pushover analysis. Three key parameters including the stiffness degradation factor, the activation strain, and the initial axial stiffness of the SC-TOBs, are investigated thoroughly because of their unique characteristics and tunability compared with traditional bracing systems. Identical steel frames equipped with BRBs are also designed and examined for comparison purposes.

## 2. Configuration and Mechanics of the SC-TOB

A schematic of the SC-TOB [36, 37] showing its basic function is shown in Figure 1. The brace mainly consists of three parts: a high-strength steel (HSS) cable as a bracing element, a frictional device (FD) to dissipate seismic energy, and PT tendons to produce a full self-centering hysteresis. One end of the PT tendons is anchored to the blocking plate, and the other end passes around the pulley and connects with the FD after a certain pretension is imposed.

The mechanics of the SC-TOB can be explained using the analytical model presented in Figure 2: the PT tendons, FD, and HSS cable are idealized as springs with axial stiffnesses  $k_t$ ,  $k_f$ , and  $k_c$ , respectively, and the frictional resistance of the FD is  $F$ ; the pretension of the PT tendons is  $T_0$ . The blocking plate  $R$  is used to balance the pretension and restrict the left movement of the FD.

The hysteretic behavior of the SC-TOB is illustrated in Figure 3. When the value of the lateral load  $P$  is less than the sum of the pretension force and the frictional resistance (i.e.,  $P < T_0 + F$ ), only the HSS cable works (Stage o-a), and the initial axial stiffness of the SC-TOB is  $k_1$ :

$$k_1 = k_c = \frac{E_c A_c}{l_c}, \quad (1)$$

where  $E_c$ ,  $A_c$ , and  $l_c$  are Young's modulus, cross-sectional area, and original length of the HSS cable, respectively.

As  $P$  increases to  $P = T_0 + F$ , the energy dissipative mechanism provided by FD is activated. Defining the load  $P$  at Event  $a$  as the activation load  $P_a$ ,

$$P_a = T_{t,0} + F. \quad (2)$$

At Stage a-b, the stiffness of the SC-TOB decreases significantly from  $k_1$  to the postactivation stiffness,  $k_2$ , given by

$$k_2 = \left( \frac{1}{k_t} + \frac{1}{k_f} + \frac{1}{k_c} \right)^{-1}. \quad (3)$$

As the cross-sectional area of the friction device is much greater than that of the cable and tendon, while the length of the friction device is much smaller than that of the cable and tendon, i.e.,  $k_f \gg \max\{k_t, k_c\}$ , equation (3) can be revised as

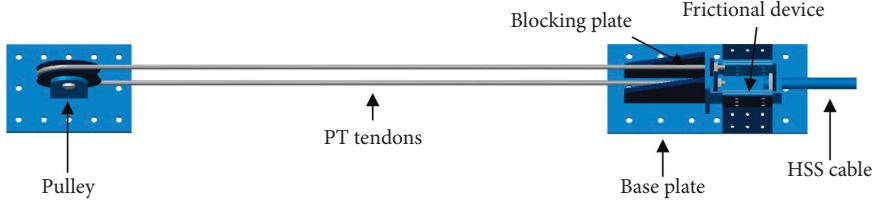


FIGURE 1: Schematic of SC-TOB.

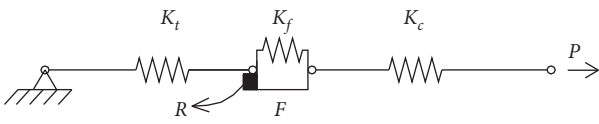


FIGURE 2: Analytical model of SC-TOB.

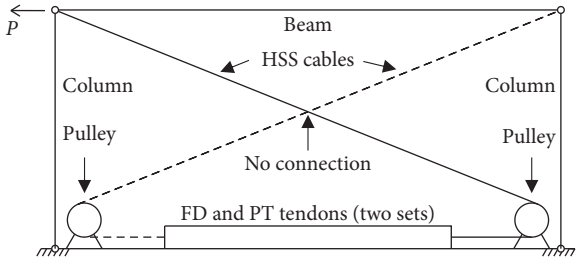


FIGURE 4: Arrangement of SC-TOB.

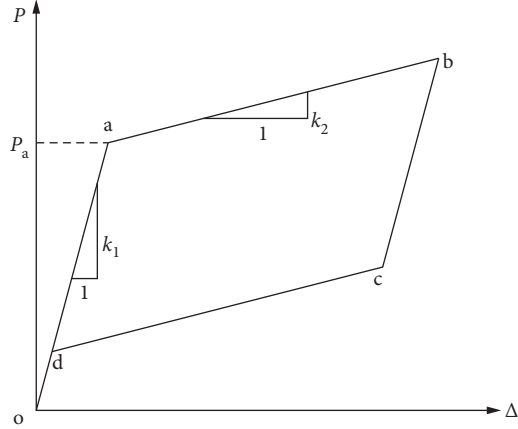


FIGURE 3: Hysteretic behavior of SC-TOB.

$$k_2 = \left( \frac{1}{k_t} + \frac{1}{k_c} \right)^{-1}. \quad (4)$$

When unloading begins at Event *b*, the friction will first reduce gradually from *F* to zero and then increase in the opposite direction to  $-F$  at Event *c*. During this stage, only the HSS cable works, so the stiffness of the SC-TOB is recovered to  $k_1$ . As *P* further unloads (Stage *c-d*), the SC-TOB is capable of returning to its initial position by the sufficient restoring force produced by the PT tendons as long as  $T_{t,0}$  is no less than *F*. During this stage, the stiffness of the SC-TOB is reduced again to the postactivation stiffness  $k_2$ . With continued unloading, the tension force of the HSS cable decreases to zero after load removal and the stiffness of the SC-TOB during Stage *d-o* is once again recovered to  $k_1$ .

A structure incorporating the SC-TOBs in a frame bay is described in Figure 4, in which the solid line indicates an active HSS cable and the dotted line indicates a loose one. The pulleys mounted on the beam near the beam-column connections, which are not part of an SC-TOB, are used to guide the HSS cables.

### 3. Building Design and Modeling

**3.1. Building Design.** The 9- and 16-story prototype buildings, which have an identical plan configuration and a constant story height of 3.9 m, are braced with BRBs or SC-TOBs, as shown in Figure 5, in which both types of bracing elements are denoted by the dotted lines. Figure 6 illustrates the elevation view of the 9-story SC-TOB frames (SC-TOBFs) and BRB frames (BRBFs), in which all the beams are pinned to the columns. The load information considered in this design is listed in Table 1.

In view of the symmetrical plan dimensions of the prototype buildings, the torsion effect is neglected and thereby the lateral force will be equally distributed to the corresponding braced frames, allowing for a 2D analysis to be performed in lieu of 3D analysis for efficiency and simplicity purposes. The modal analysis comparison results, as shown in Table 2, confirms that the 2D models will suffice for the following investigation.

**3.2. Simulation of SC-TOB.** The structural analysis program SAP2000 [38] is utilized for simulating the SC-TOB. A multilinear elastic element (MEE) is used to model the PT tendons behavior, as shown in Figure 7(a). The force-deformation relationship is nonlinear, but it is elastic. This means that the element loads and unloads along the same curve, and no energy is dissipated. The friction mechanism is modeled by using a multilinear plastic element (MPE), as shown in Figure 7(b). Note that for both elements, only the second-stage curves with a softened stiffness are valid to model the required behaviors of the PT tendons and FD, so a negligible first-stage deformation has to be specified. The HSS cable could have been simulated using the linear elastic frame element (LEFE), but a severe numerical oscillation would occur when the MEE or MPE is connected directly with LEFE due to incompatibility between

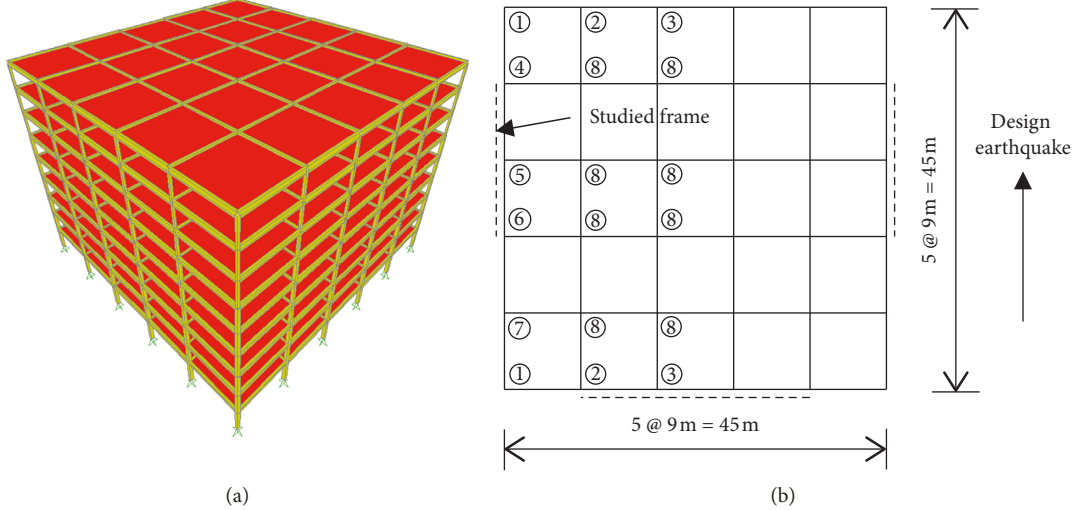


FIGURE 5: Prototype buildings. (a) 3D model for the 9-story building and (b) plan view.

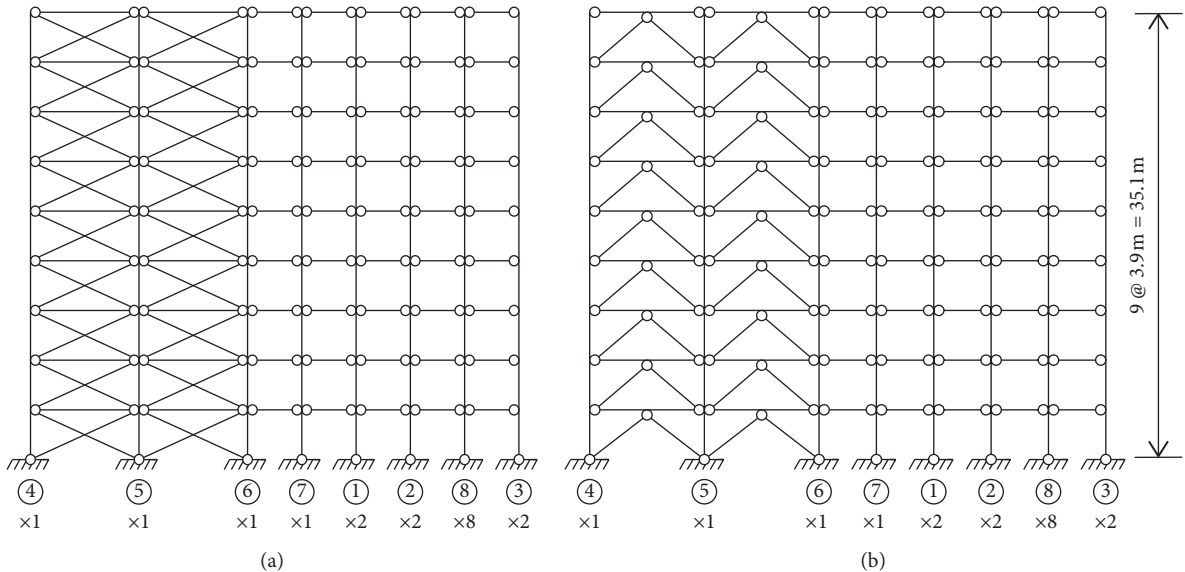


FIGURE 6: Elevation view of 9-story prototype buildings: (a) SC-TOBFs and (b) BRBFs.

TABLE 1: Load information.

	Floor	Dead	4.5 kN/m <sup>2</sup>
		Live	4.0 kN/m <sup>2</sup>
Gravity loads	Roof	Dead	5.0 kN/m <sup>2</sup>
		Live	2.0 kN/m <sup>2</sup>
	Exterior walls	Dead	10.0 kN/m
Seismic precautionary intensity			8
Seismic load data	Site classification		III
	Basic acceleration of ground motion		0.20 g

linear and nonlinear elements. Therefore, the MEEs with a sufficiently long first-stage curve are also used herein for the cables to ensure that the cable would always work within this stage. The target hysteresis and integrated

model of the SC-TOB are shown in Figures 7(c) and 7(d), respectively.

The pulley is simulated using five hinged frame elements within the dotted circle, as shown in Figure 8, in which nodes 1, 2, and 3 are located around the center point O. Because the pulley is almost a rigid body in real structures, the axial stiffness of each frame element has to be specified sufficiently large. A “body constraint” is specified to node O and its vertical projection O' on the beam to ensure that both the nodes would move together as a 3D rigid body.

The combination of all the elements associated with the SC-TOB simulation is illustrated in Figure 9, in which C' and D' on the beam are the vertical projection of nodes C and D, respectively. Body constraints are also specified for C and C', and D and D', except that the translational degree of freedom of node C is released.

TABLE 2: Comparison of modal analysis.

Story number	BRBFs				SC-TOBFs			
	9 3D	9 2D	16 3D	16 2D	9 3D	9 2D	16 3D	16 2D
Mode 1	1.820 s	1.784 s	2.638 s	2.583 s	2.729 s	2.696 s	3.579 s	3.508 s
MPMR	0.780	0.777	0.737	0.737	0.790	0.790	0.765	0.769
Mode 2	0.652 s	0.639 s	0.903 s	0.886 s	0.955 s	0.945 s	1.208 s	1.190 s
MPMR	0.140	0.143	0.160	0.160	0.120	0.120	0.128	0.130
Mode 3	0.368 s	0.361 s	0.497 s	0.490 s	0.551 s	0.547 s	0.677 s	0.674 s
MPMR	0.042	0.042	0.045	0.045	0.040	0.040	0.041	0.042

MPMR: modal participating mass ratio.

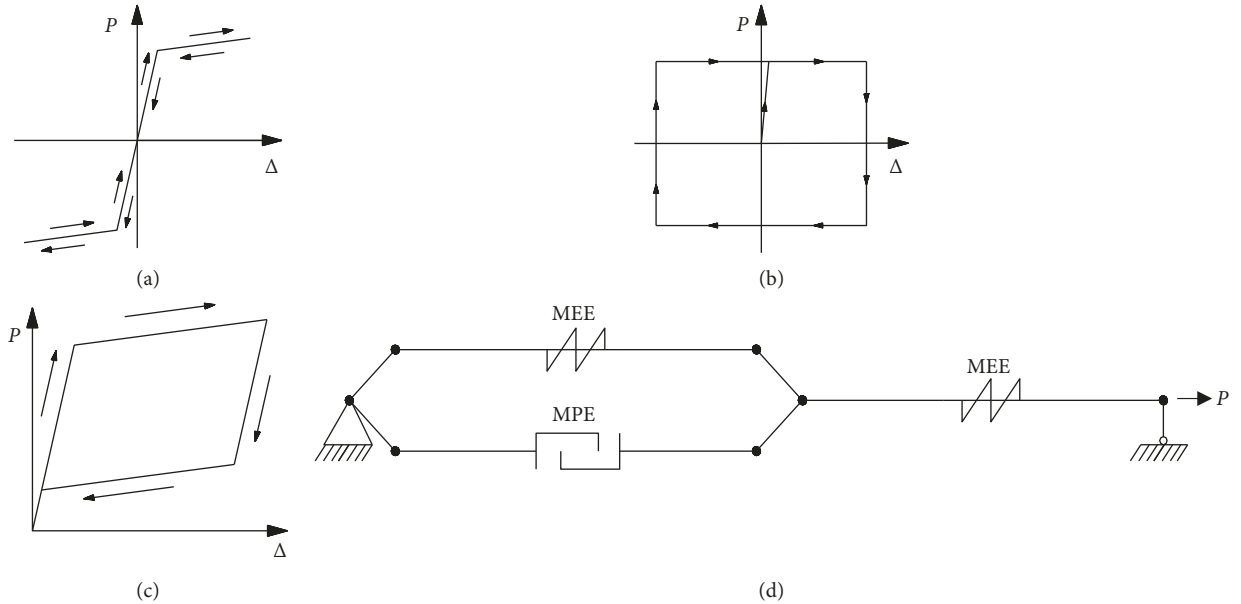


FIGURE 7: Simulation of SC-TOB: (a) MEE, (b) MPE, (c) target hysteresis, and (d) integrated model.

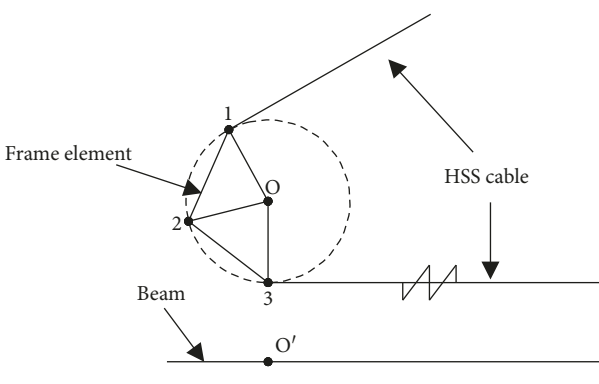


FIGURE 8: Simulation of the pulley.

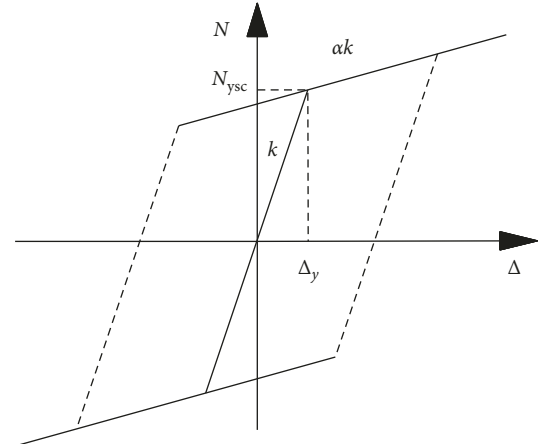


FIGURE 10: The MPE for BRB simulation.

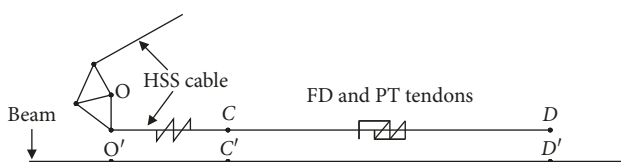


FIGURE 9: Combination of elements for SC-TOB simulation.

**3.3. Simulation of BRB.** The MPE with kinematic hysteresis is introduced to simulate the BRB behavior [38], as shown in Figure 10, in which  $N_{ysc}$ ,  $\Delta_y$ ,  $k$ , and  $\alpha$  are the yield capacity, yield deformation, axial stiffness, and postyield stiffness ratio of the steel core, respectively. In this paper,  $\alpha$  is taken as 3%.

TABLE 3: Geometric detail of beams and columns of the 9-story frames.

Story	Unbraced frames		Braced frames	
	Beam	Column	Beam	Column
7–9		□300 × 300 × 10 × 10	H800 × 300 × 14 × 26	□300 × 300 × 10 × 10
4–6	H700 × 300 × 13 × 24	□400 × 400 × 14 × 14	H850 × 300 × 17 × 31	□400 × 400 × 20 × 20
1–3		□450 × 450 × 20 × 20	H900 × 300 × 18 × 34	□500 × 500 × 25 × 25

TABLE 4: Geometric detail of beams and columns of the 16-story frames.

Story	Unbraced frames		Braced frames	
	Beam	Column	Beam	Column
13–16		□350 × 350 × 10 × 10	H850 × 300 × 16 × 27	□400 × 400 × 15 × 15
9–12	H700 × 300 × 13 × 24	□400 × 400 × 20 × 20	H900 × 300 × 18 × 34	□600 × 600 × 30 × 30
5–8		□500 × 500 × 25 × 25	H1000 × 300 × 21 × 40	□800 × 800 × 40 × 40
1–4		□650 × 650 × 25 × 25	H1100 × 400 × 20 × 36	□850 × 850 × 45 × 45

TABLE 5: Geometric detail of braces of the 9-story frames.

Story	SC-TOB			Core Area (mm <sup>2</sup> )
	PT tendons	Diameter (mm)	Area (mm <sup>2</sup> )	
7–9		33.9	903	3510
4–6		38.8	1182	5130
1–3		43.6	1493	6120

TABLE 6: Geometric detail of braces of the 16-story frames.

Story	SC-TOB			Core Area (mm <sup>2</sup> )
	PT tendons	Diameter (mm)	Area (mm <sup>2</sup> )	
13–16		53.3	2231	5940
9–12		58.2	2660	8280
5–8		58.2	2660	9810
1–4		63.0	3117	11070

TABLE 7: Summary of selected material properties.

Structural member	Material	Yield stress, $f_y$ (MPa)	Young's modulus, $E$ (GPa)
Beam and column	Q345 steel	345	200
SC-TOB	HSS cable	835	200
BRB core	PT tendon	2267	74
		140	200

The design axial strength of the brace,  $N$ , is determined under the frequently occurred earthquake (FOE) condition, and according to

$$N = 0.9A f_y, \quad (5)$$

the cross-sectional area of the steel core,  $A$ , can be calculated, where  $f_y$  is the yield stress of the core. The yield capacity of the brace,  $N_{ysc}$ , can be calculated by

$$N_{ysc} = \eta_y f_y A, \quad (6)$$

where  $\eta_y$  is the overstrength factor of the core. The maximum axial strength of the brace,  $N_{y\max}$ , can be calculated by

$$N_{y\max} = \omega N_{ysc}, \quad (7)$$

where  $\omega$  is the strain-hardening adjustment factor.

**3.4. Design Information of the Prototype Buildings.** The criterion used for the SC-TOBFs design is that all member force demands and the story drift must satisfy the design objectives under the design basis earthquake. With the increase of earthquake intensity, the seismic forces induced in the load-resisting elements such as beams, columns, and braces in the braced bays increase nonlinearly, whereas that in the unbraced bays remain nearly unchanged. Hence,

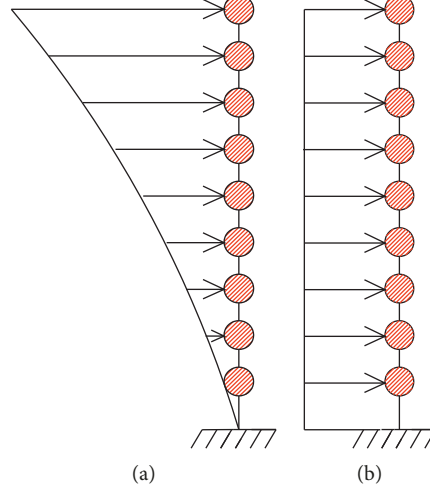


FIGURE 11: Lateral load distributions: (a) parabolic distribution (LD-1) and (b) uniform distribution (LD-2).

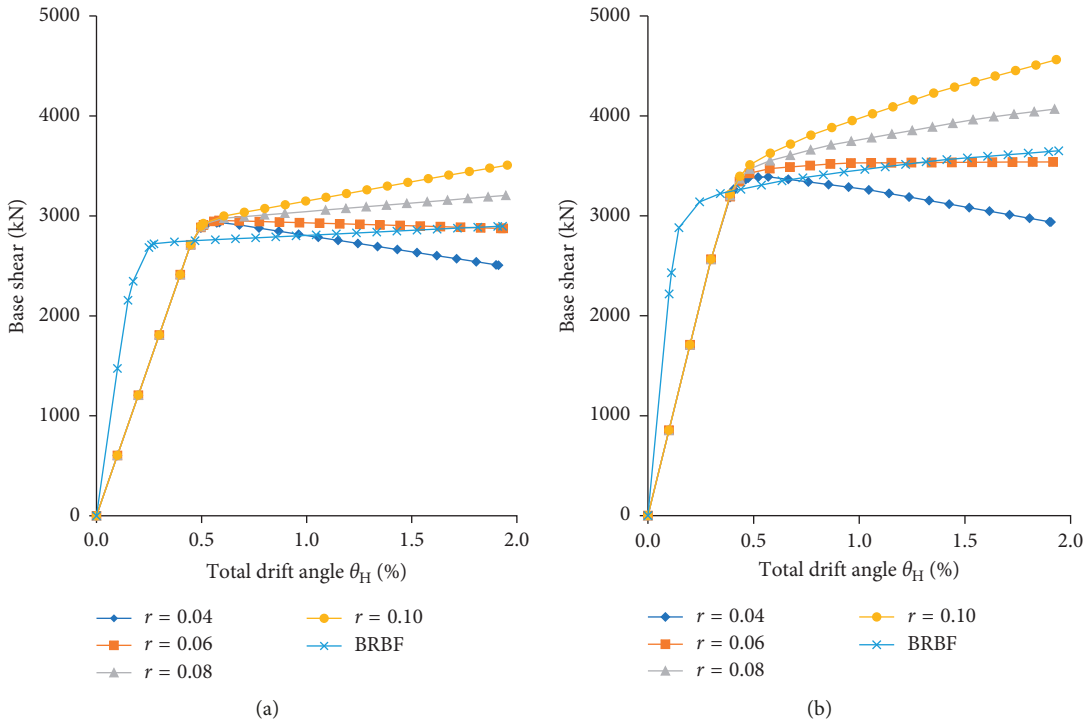


FIGURE 12: The effects of  $r$  on the base shear response of 9-story SC-TOBFs: (a) LD-1 and (b) LD-2.

different limits of “demand-capacity ratio” are specified: 0.5 and 0.8 for the elements in braced and unbraced frames, respectively, so as to ensure that all of them remain essentially elastic or achieve full self-centering even under the most severe load condition in this analysis. The BRB components are designed according to the design codes [39–42]. The step-by-step design procedure of the SC-TOB could be referred to the literature [37], and the ratio of  $T_{t,0}$  and  $F$  is set at 1.05 for all SC-TOBs throughout this paper. The geometric and material properties of all the elements

are listed in Tables 3–7. A strength check is performed through the structure after every pushover procedure, confirming that all the structural elements remain elastic without any damage in the analyses of the following section.

#### 4. Parametric Study

*4.1. Lateral Load Distribution.* As illustrated in Figure 11, two lateral load distributions, the parabolic distribution

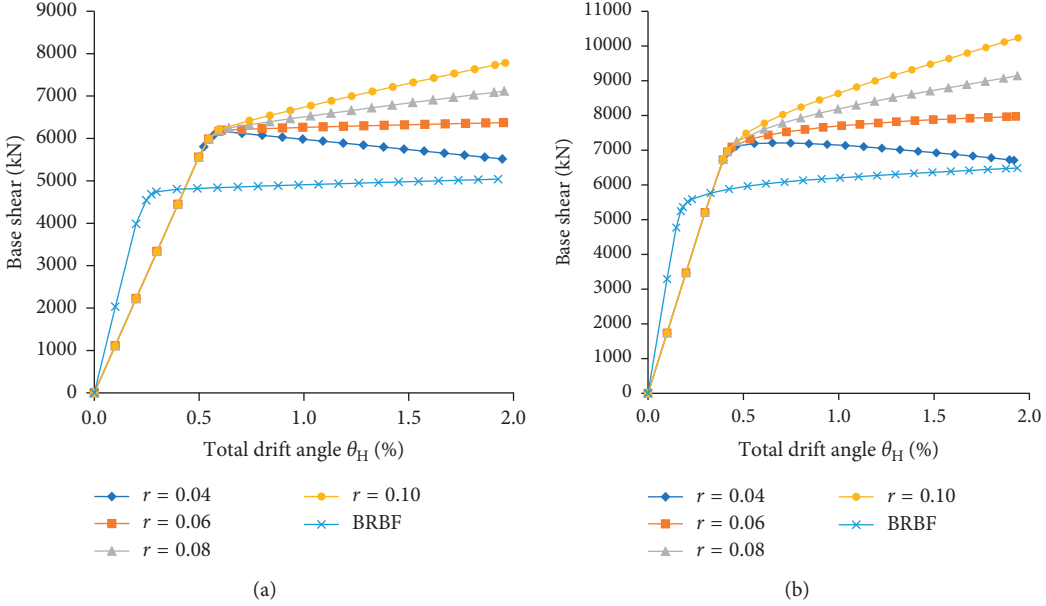


FIGURE 13: The effects of  $r$  on the base shear response of 16-story SC-TOBFs: (a) LD-1 and (b) LD-2.

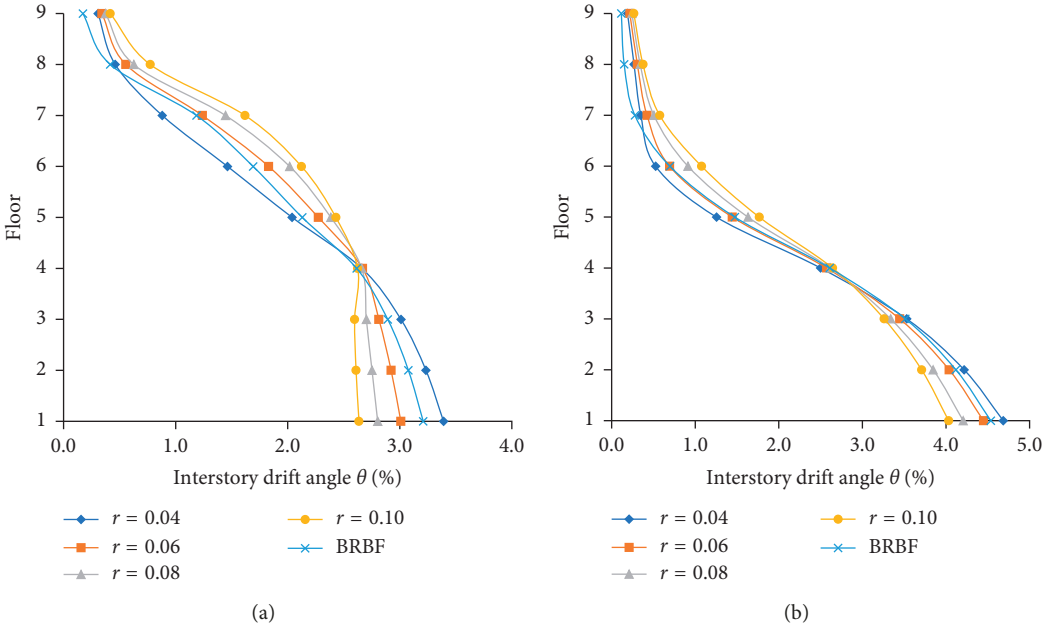


FIGURE 14: The effects of  $r$  on the interstory drifts of 9-story SC-TOBFs: (a) LD-1 and (b) LD-2.

(denoted as “LD-1”) and the uniform distribution (denoted as “LD-2”), are adopted as suggested in ASCE 7-10 [31]. These distributions can be expressed as

$$\Delta F_i = \frac{w_i h_i^k}{\sum_{j=1}^n w_j h_j^k} \Delta V_b, \quad (8)$$

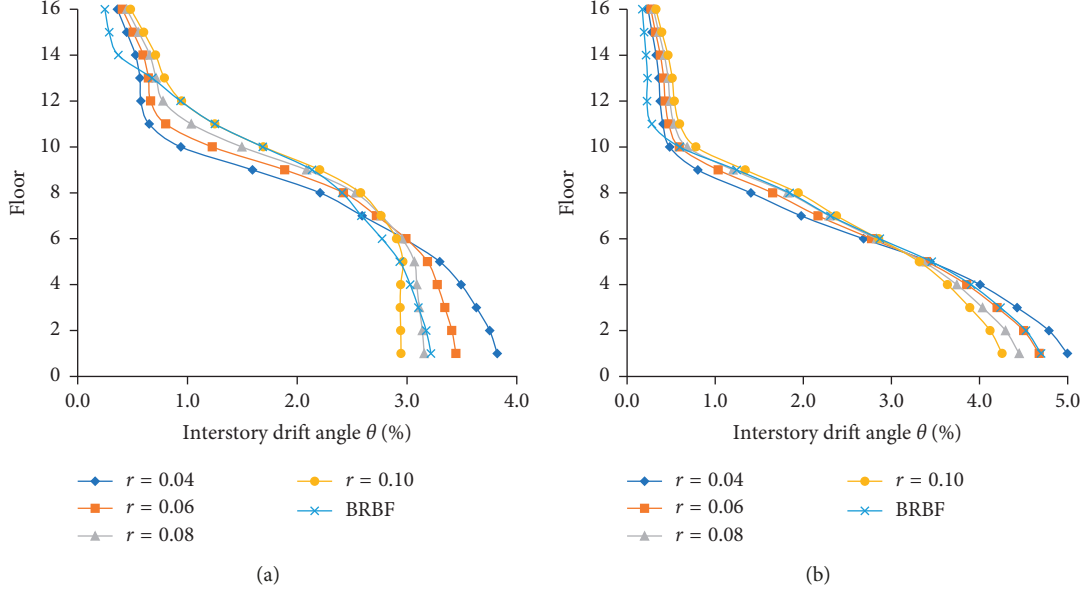
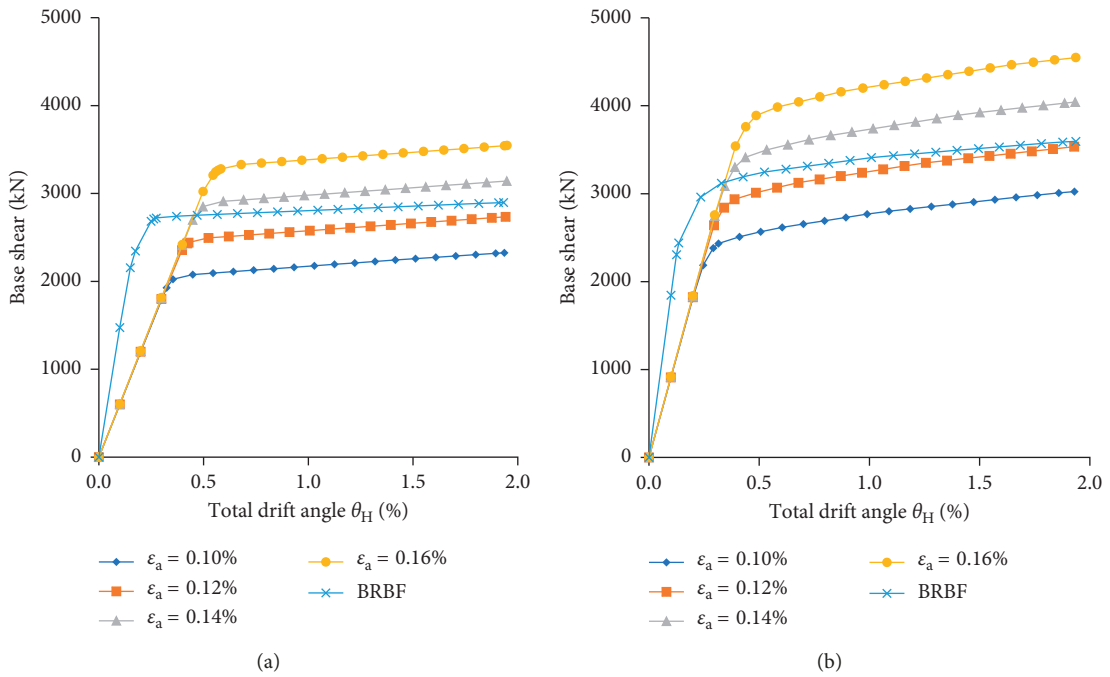
$$\Delta F_i = \frac{w_i}{\sum_{j=1}^n w_j} \Delta V_b, \quad (9)$$

where  $\Delta F_i$  is the lateral load increment assigned to floor level  $i$ ,  $\Delta V_b$  is the base shear increment of the structure,  $w_i$  and  $w_j$  are the building weights located on floor level  $i$  and  $j$ ,

respectively,  $h_i$  and  $h_j$  are the heights from the base to floor level  $i$  and  $j$ , respectively,  $n$  is the total number of stories,  $k = 2.0$  for  $T \geq 2.5$  s,  $k = 1.0$  for  $T \leq 0.5$  s, and linear interpolation is used to select the values of  $k$  between  $0.5$  s  $< T < 2.5$  s.

An incremental static procedure for both load distributions is performed until a target displacement, which is represented by the total drift angle of the prototype buildings,  $\theta_H$  (as expressed in equation (10)), is exceeded:

$$\theta_H = \frac{\Delta_H}{H}, \quad (10)$$

FIGURE 15: The effects of  $r$  on the interstory drifts of 16-story SC-TOBFs: (a) LD-1 and (b) LD-2.FIGURE 16: The effects of  $\varepsilon_a$  on the base shear response of 9-story SC-TOBFs: (a) LD-1 and (b) LD-2.

where  $\Delta_H$  is the horizontal displacement of the control node located at the center of mass of the roof and  $H$  is the total height of the structure. In this paper,  $\theta_H$  is taken as 2% corresponding to the limit prescribed by the building codes [41, 42].

**4.2. Effects of Stiffness Degradation Factor  $r$ .** The stiffness degradation factor,  $r$ , as defined by the ratio of the

postactivation stiffness  $k_2$  to the initial axial stiffness  $k_1$  of the SC-TOB, is expressed as

$$r = \frac{k_2}{k_1}. \quad (11)$$

If  $r$  is too large, the seismic forces induced in the brace and adjacent structural members will increase rapidly, which is neither economical nor safe. But if  $r$  is too small (e.g., 3% for BRB [43]), damage concentration would be induced at

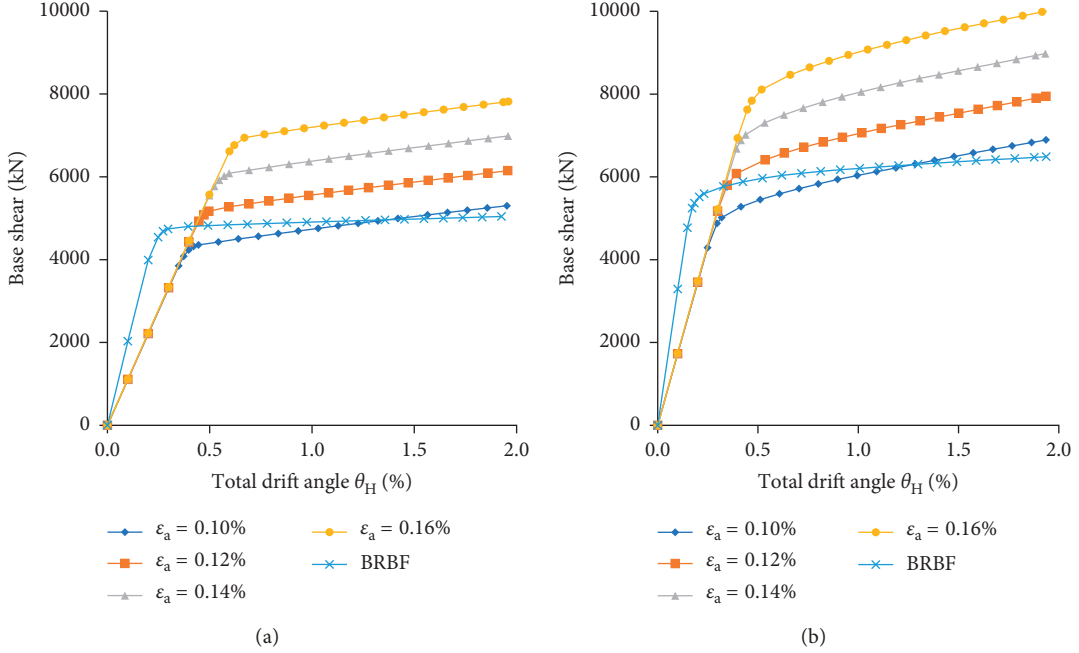


FIGURE 17: The effects of  $\epsilon_a$  on the base shear response of 16-story SC-TOBFs: (a) LD-1 and (b) LD-2.

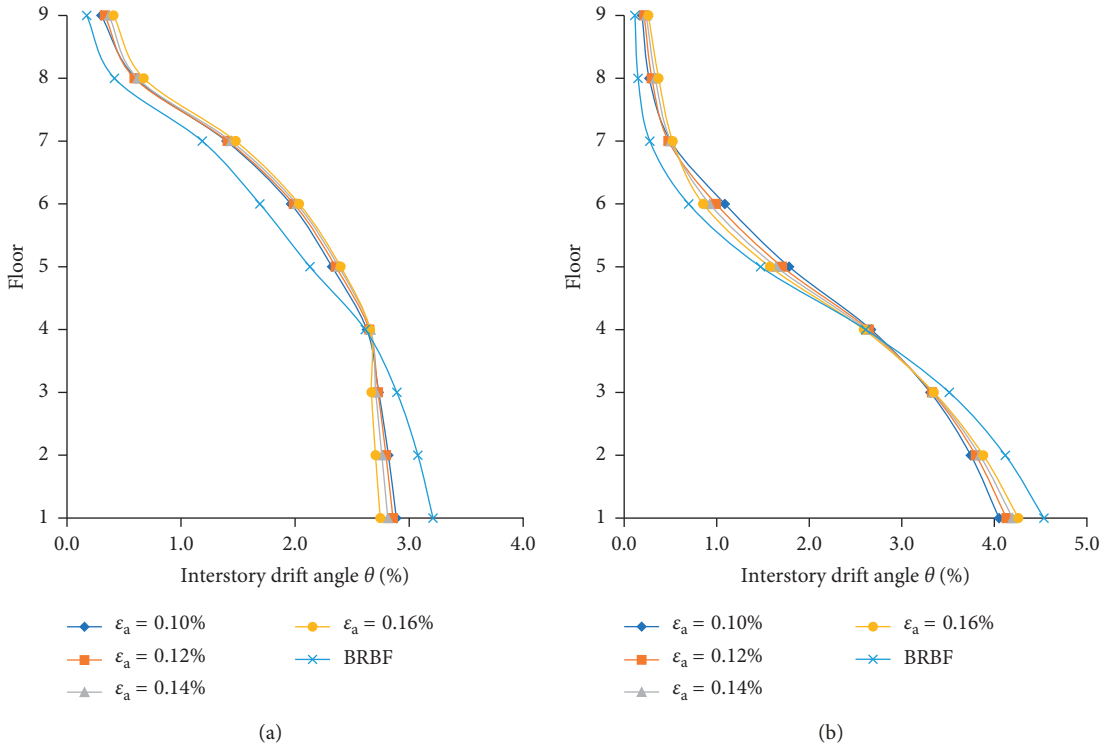


FIGURE 18: The effects of  $\epsilon_a$  on the interstory drifts of 9-story SC-TOBFs: (a) LD-1 and (b) LD-2.

certain stories, thus limiting the capacity of the structure to redistribute the demand along the height. Furthermore, the  $P$ -delta effects will also elevate the collapse risk. Hence,  $r$  varying from 4% to 10% is investigated in this section.

**4.2.1. Base Shear Response.** The effects of  $r$  on the base shear response of SC-TOBFs with 9 and 16 stories are shown in Figures 12 and 13, respectively. With increasing  $r$  from 4% to 10%, the second stiffness of the structure  $K_2$  increases

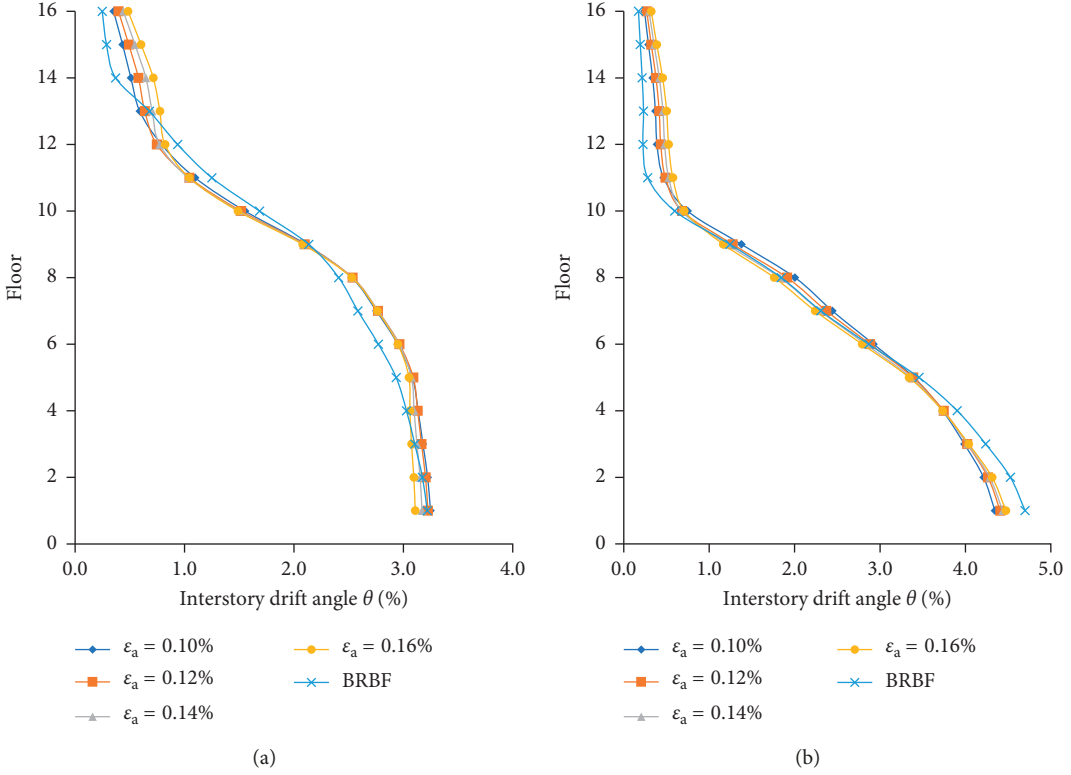


FIGURE 19: The effects of  $\varepsilon_a$  on the interstory drifts of 16-story SC-TOBFs: (a) LD-1 and (b) LD-2.

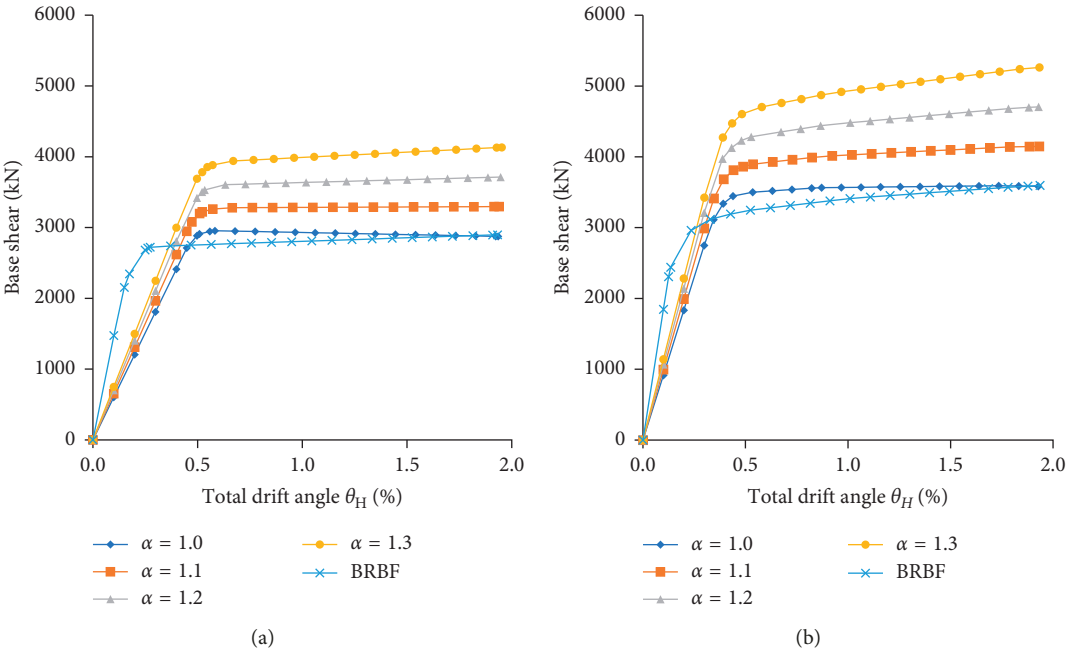


FIGURE 20: The effects of  $\alpha$  on the base shear response of 9-story SC-TOBFs: (a) LD-1 and (b) LD-2.

significantly, and the negative  $K_2$  corresponding to  $r = 4\%$  is improved. The changes in  $r$  have no effect on the first stiffness  $K_1$ , the activation load  $P_A$ , and the activation total drift angle  $\theta_A$  of the structure. The SC-TOBFs exhibit a smaller  $K_1$  than BRBFs do, because SC-TOBs can make full

use of high-strength materials such that the seismic response of structures is mitigated because of a prolonged fundamental period. Besides, unlike BRBFs for which the stiffness degrades due to the yielding of the steel core,  $K_2$  of SC-TOBFs is determined by  $k_t$ , which makes  $K_2$  significantly

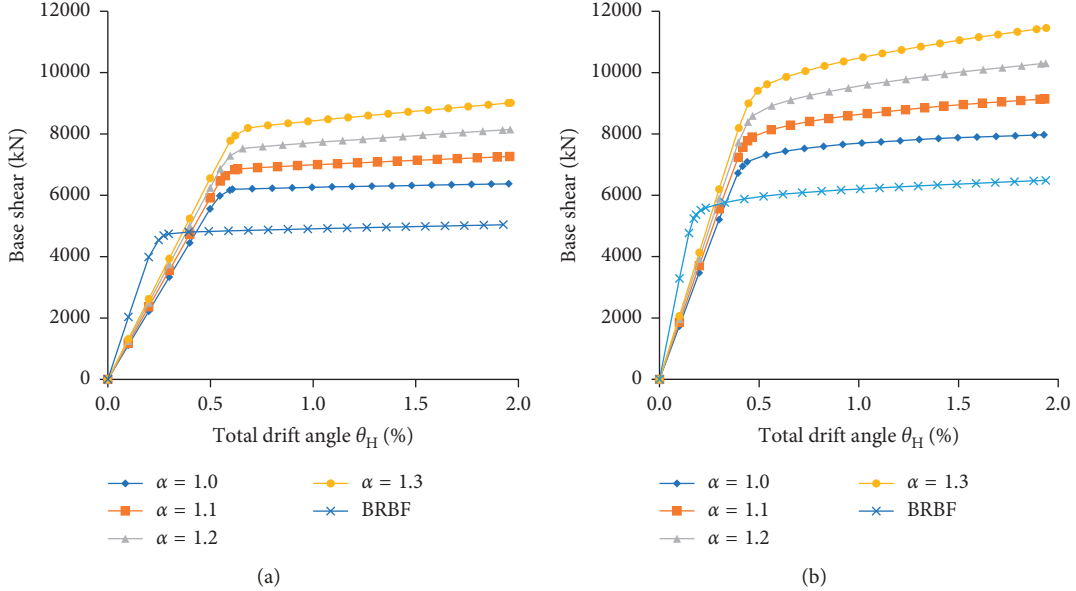


FIGURE 21: The effects of  $\alpha$  on the base shear response of 16-story SC-TOBFs: (a) LD-1 and (b) LD-2.

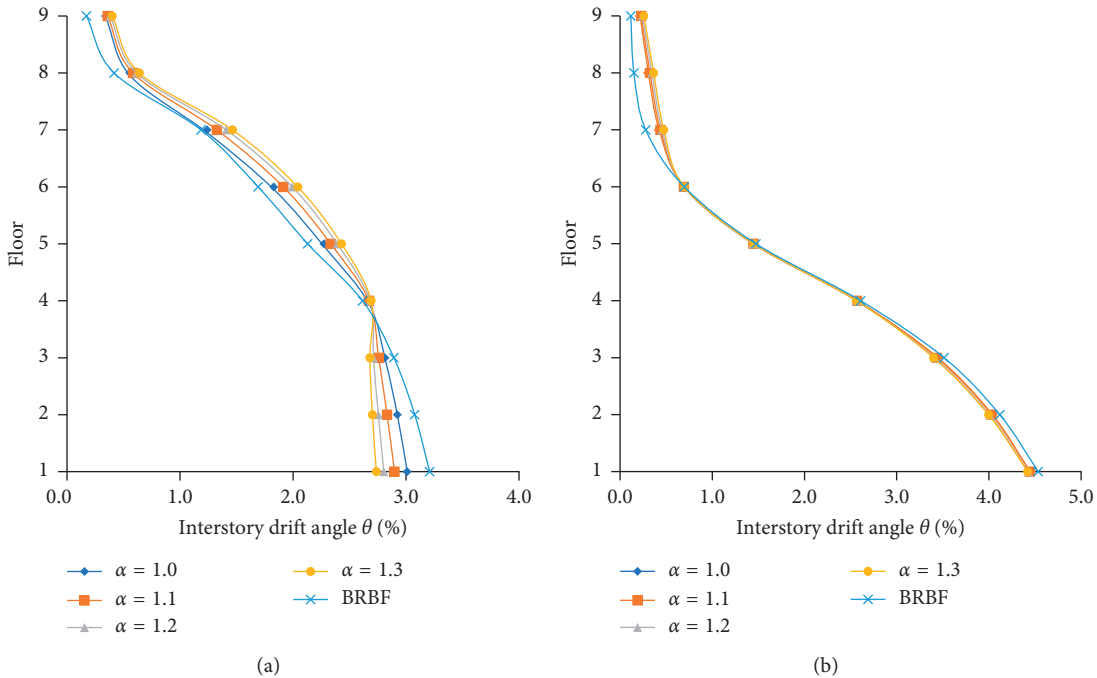


FIGURE 22: The effects of  $\alpha$  on the interstory drifts of 9-story SC-TOBFs: (a) LD-1 and (b) LD-2.

lower than  $K_1$  and plays a similar role in yielding or ductility. This provides a flexible design space for the SC-TOBFs to achieve a required postactivation performance by varying  $r$ .

**4.2.2. Interstory Drift Response.** The effects of  $r$  on the interstory drift of SC-TOBFs with 9 and 16 stories are shown in Figures 14 and 15, respectively. Basically, both SC-TOBFs and BRBFs show the same tendency in terms of interstory drifts, decreasing from bottom to top. With the increase of  $r$ ,

the interstory drifts of the lower part of the SC-TOBFs decrease gradually while the drifts of the upper part increase, indicating that the distribution of drifts over the building could be improved by selecting a relatively large  $r$ .

**4.3. Effects of Activation Strain  $\varepsilon_a$ .** The activation strain,  $\varepsilon_a$ , defined as the strain of the HSS cable when an SC-TOB reaches its activation load  $P_a$ , can be expressed as

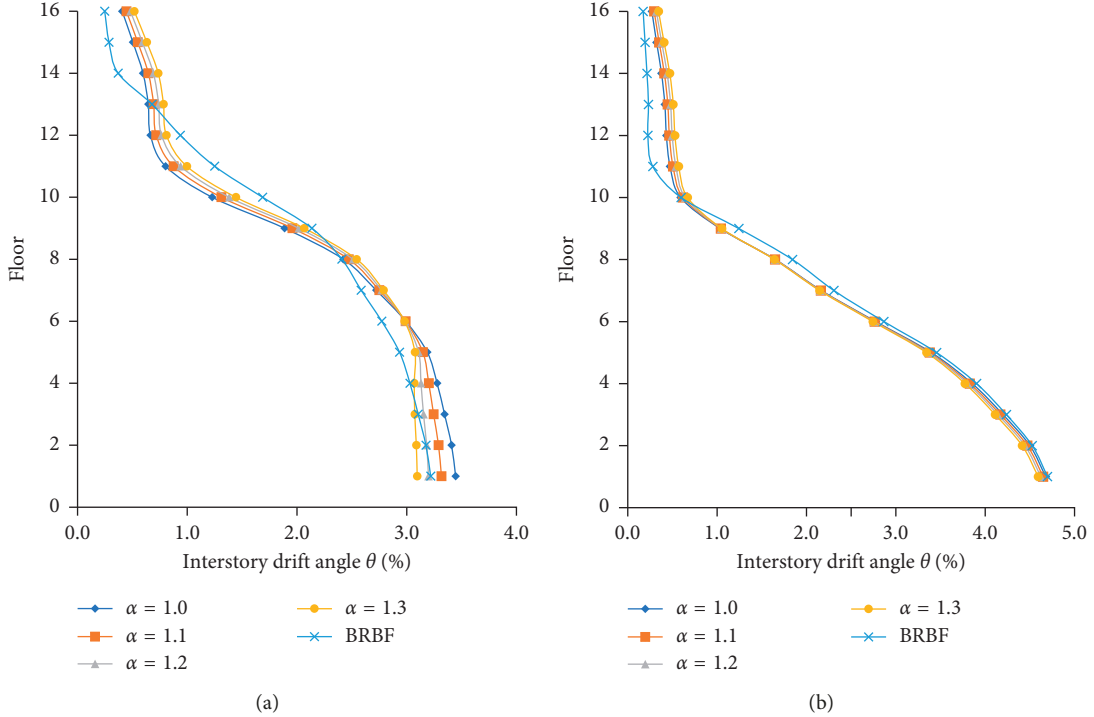


FIGURE 23: The effects of  $\alpha$  on the interstory drifts of 16-story SC-TOBFs: (a) LD-1 and (b) LD-2.

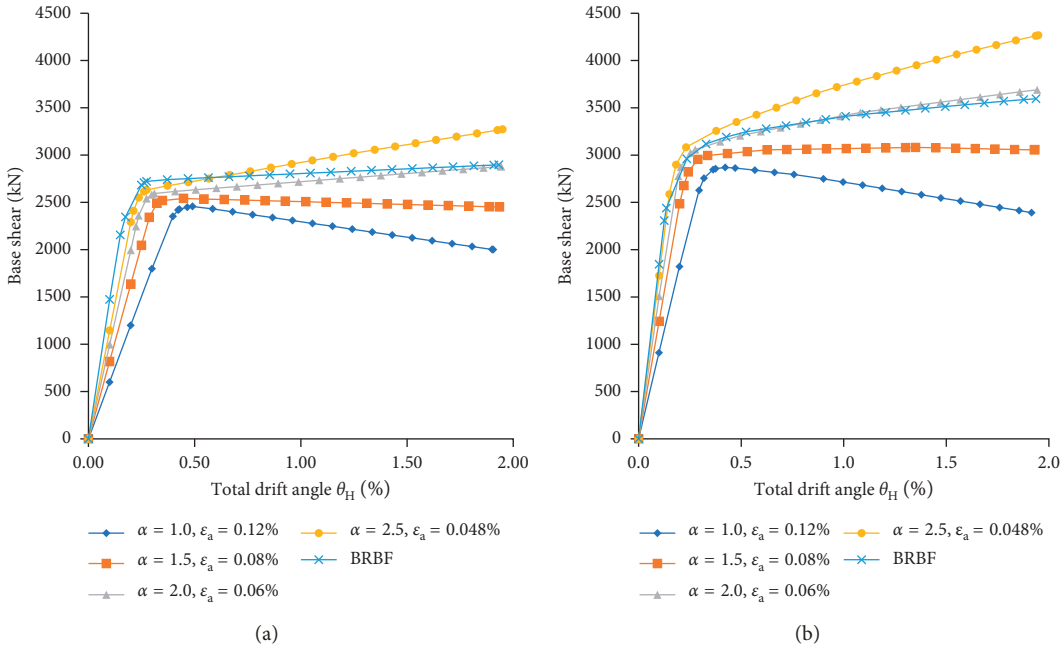


FIGURE 24: The effects of  $\varepsilon_a$  and  $\alpha$  on the base shear response of 9-story SC-TOBFs: (a) LD-1 and (b) LD-2.

$$\varepsilon_a = \frac{\Delta_a}{l_c}, \quad (12)$$

where  $\Delta_a$  is the activation deformation of the SC-TOB corresponding to  $P_a$ . Since  $\varepsilon_a$  determines the deformation state of the structure when the SC-TOB starts to work, it permits designers to advance or delay the activation by

specifying a suitable value accordingly. For BRBs, the activation strain depends on the yield strain of their steel core, which is made of Q160LY with yield strain of 0.07% in this paper.

**4.3.1. Base Shear Response.** The effects of  $\varepsilon_a$  on the base shear response of SC-TOBFs with 9 and 16 stories are shown in

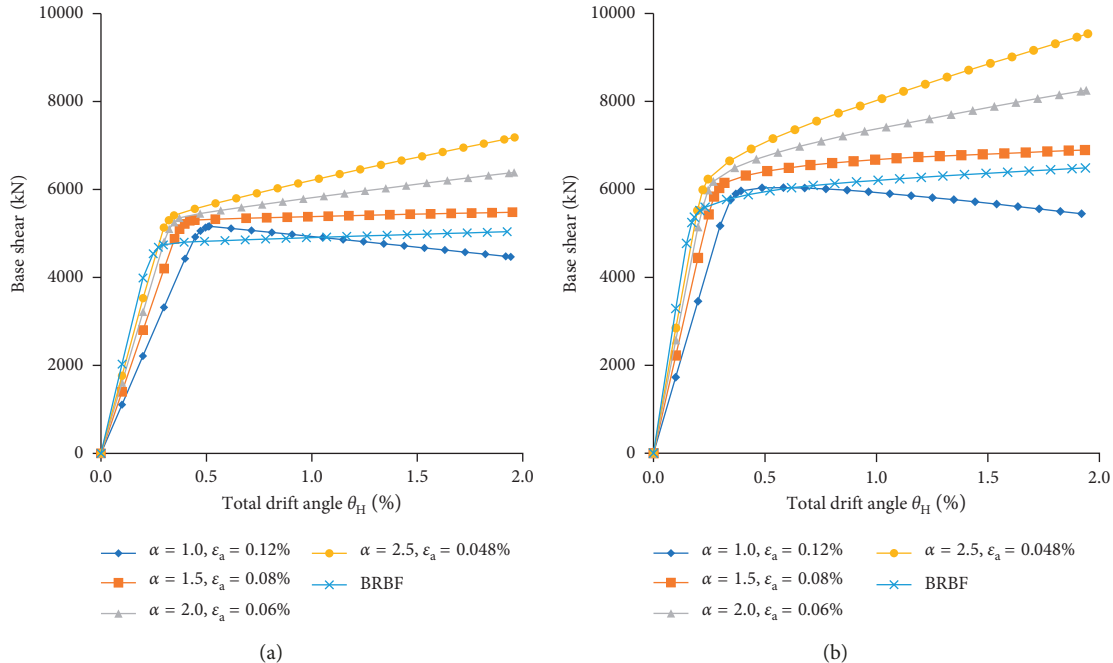


FIGURE 25: The effects of  $\varepsilon_a$  and  $\alpha$  on the base shear response of 16-story SC-TOBFs. (a) LD-1. (b) LD-2.

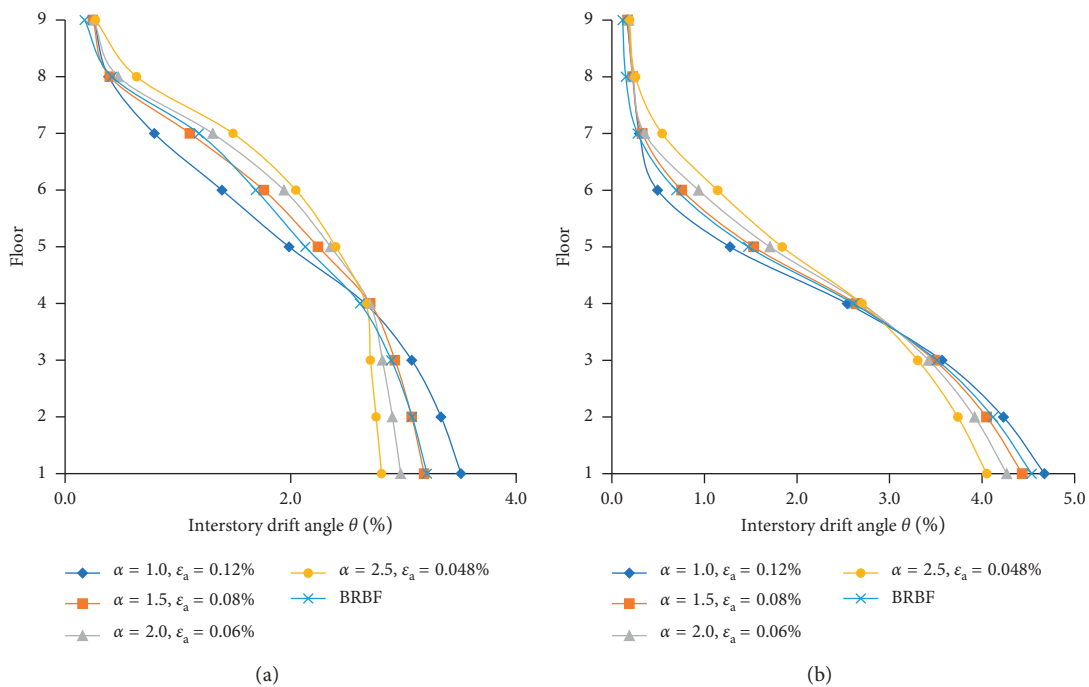


FIGURE 26: The effects of  $\epsilon_a$  and  $\alpha$  on the interstory drifts of 9-story SC-TOBFs: (a) LD-1 and (b) LD-2.

Figures 16 and 17, respectively. With the increase of  $\varepsilon_a$ , the activation deformation  $\Delta_A$  and activation load  $P_A$  of the structure increase gradually. However, the changes in  $\varepsilon_a$  have no effect on  $K_1$  and  $K_2$  of the structure. Due to the limitations of material property for the core, BRBFs have a constant  $\Delta_A$ . Compared with BRBFs, SC-TOBFs can flexibly

control the deformation state when the structures enter the postactivation stage by adjusting the value of  $\varepsilon_a$ .

**4.3.2. Interstory Drift Response.** The effects of  $\varepsilon_a$  on the interstory drifts of SC-TOBFs with 9 and 16 stories are

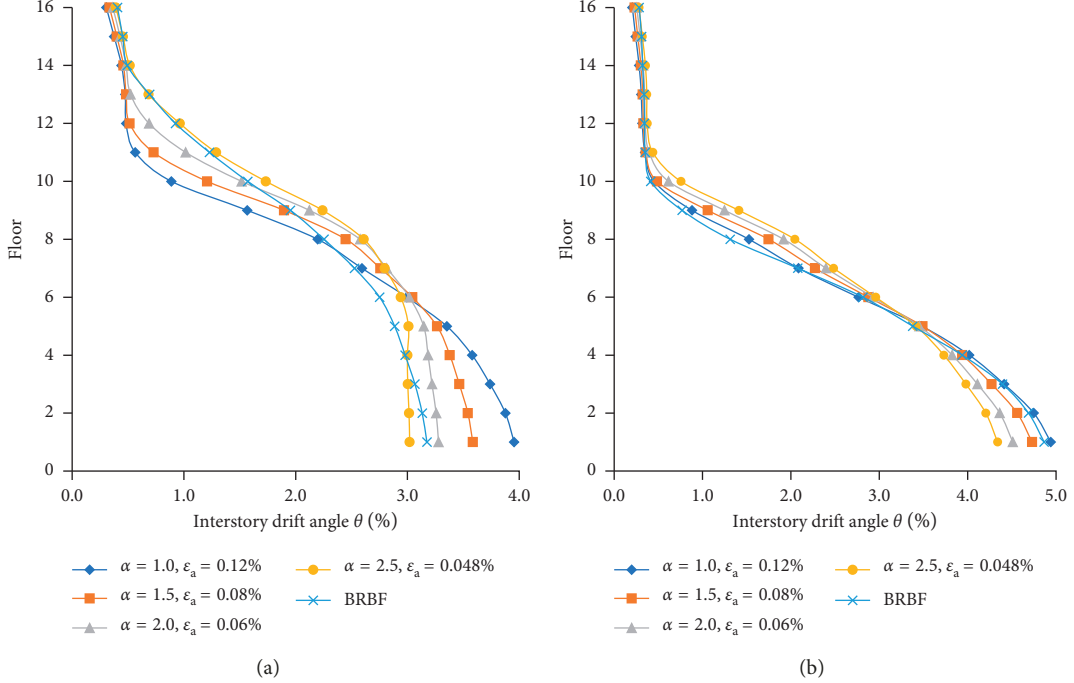


FIGURE 27: The effects of  $\varepsilon_a$  and  $\alpha$  on the interstory drifts of 16-story SC-TOBFs: (a) LD-1 and (b) LD-2.

shown in Figures 18 and 19, respectively. For the SC-TOBFs, the changes in  $\varepsilon_a$  have a very limited effect on the distribution of interstory drifts of each story. This is primarily because  $\varepsilon_a$ , governing the activation deformation state of the structure, is very small compared with the strain of the SC-TOB at the end of analysis, such that it tends to display a negligible impact on the final interstory drift response.

**4.4. Effects of Initial Axial Stiffness  $k_1$ .** To investigate the effects of  $k_1$  on SC-TOBFs, a stiffness amplification factor  $\alpha$  is introduced as

$$\alpha = \frac{k'_1}{k_1}, \quad (13)$$

where  $k_1$  is the initial axial stiffness of a specific SC-TOB selected from Tables 5 and 6 and  $k'_1$  is the amplified stiffness of the corresponding brace. Note that  $r$  should remain constant in this section.

**4.4.1. Base Shear Response.** The effects of  $\alpha$  on the base shear response of SC-TOBFs with 9 and 16 stories are shown in Figures 20 and 21, respectively. With increasing  $\alpha$  from 1.0 to 1.3,  $K_1$  and  $P_A$  increase continuously, while  $\Delta_A$  remain identical as designed. BRBFs have a larger  $K_1$  than SC-TOBFs, because BRBs tend to adopt low-yield steel for the brace core, resulting in larger cross sections.

**4.4.2. Interstory Drift Response.** The effects of  $\alpha$  on the interstory drifts of SC-TOBFs with 9 and 16 stories are shown in Figures 22 and 23, respectively. Under the parabolic distribution of loads (LD-1), the interstory drifts of low

stories decrease as  $\alpha$  increases, but the effect on the middle and upper stories is not remarkable. Under the uniform distribution (LD-2), the  $\alpha$  effect is negligible.

## 5. Discussion

From the results presented in Section 4, it can be found that the first-stage lateral behavior of SC-TOBFs, in terms of  $K_1$ ,  $P_A$ , and  $\Delta_A$ , is jointly determined by  $\alpha$  and  $\varepsilon_a$ . This section deals with the coupling effects of these two parameters on SC-TOBFs based on the premise that  $P_A$  is set as constant as possible for each lateral load distribution with different building heights.

**5.1. Base Shear Response.** The coupling effects of  $\alpha$  and  $\varepsilon_a$  on the base shear response of SC-TOBFs with 9 and 16 stories are shown in Figures 24 and 25, respectively. As the values of  $\alpha$  and  $\varepsilon_a$  increase and decrease, respectively, the first-stage curves of the SC-TOBFs are more and more close to that of the BRBFs, indicating that by selecting the appropriate  $\varepsilon_a$  and  $\alpha$ , SC-TOBFs can exhibit a similar first-stage performance as BRBFs.

**5.2. Interstory Drift Response.** The coupling effects of  $\alpha$  and  $\varepsilon_a$  on the interstory drifts of SC-TOBFs with 9 and 16 stories are shown in Figures 26 and 27, respectively. As the values of  $\alpha$  and  $\varepsilon_a$  increase and decrease, respectively, the drifts of the low stories decrease gradually, while the drifts of high stories increase, similarly to the  $r$  effects. Compared with BRBFs, SC-TOBFs can achieve a comparable deformation performance by selecting the appropriate  $\varepsilon_a$  and  $\alpha$ .

## 6. Conclusions

A parametric study on the seismic response of 9- and 16-story steel-framed buildings, which can be considered typical of intermediate and high-rise buildings, with SC-TOBs is numerically conducted, and the results are compared with those of BRBFs. The effects of the stiffness degradation factor  $r$ , the activation strain  $\varepsilon_a$ , and the initial axial stiffness  $k_1$  of the SC-TOBs on the lateral behavior of the SC-TOBFs are investigated thoroughly to explore the design space. The following conclusions can be drawn from this study:

- (1) An increase in  $r$  leads to a larger second stiffness of the structure,  $K_2$ , but changes in  $r$  have no significant effect on the activation load  $P_A$  or the activation deformation  $\Delta_a$  of the structure. A relatively large  $r$  is suggested to improve the distribution of drifts over the building height.
- (2) With the increase in  $\varepsilon_a$ ,  $\Delta_a$  and  $P_A$  increase gradually, but  $\varepsilon_a$  has no effect on the first stiffness of the structure  $K_1$ , and  $K_2$ , and only a slight effect on the interstory drift distribution.
- (3) With the increase in  $k_1$ ,  $K_1$  and  $P_A$  increase continuously, and the interstory drifts of the lower part of the building under the parabolic distribution of loads are reduced.
- (4) The coupling effects of an increasing  $\varepsilon_a$  and a decreasing  $\alpha$  are similar to the  $r$  effects. It is advantageous to select a large  $r$  and a small  $k_1$  simultaneously to make the drift distribution more uniform.
- (5) The SC-TOBFs are considered to be a type of performance-tunable structure, and tuning can be achieved by varying a frame's adjustable parameters. The first-stage lateral behavior of SC-TOBFs is comparable to that of BRBFs when a lower  $\varepsilon_a$  and a higher  $k_1$  are selected, and a required second-stage behavior can be obtained by specifying a suitable  $r$ .

## Data Availability

The data used to support the findings of this study are available from the corresponding author upon request.

## Conflicts of Interest

The authors declare that there are no conflicts of interest regarding the publication of this paper.

## Acknowledgments

This research was financially supported by the National Natural Science Foundation of China (Grants numbers 51708482 and 51578478), the China Postdoctoral Science Foundation (Grant number 2017M621593), and the Six Talent Peaks Project in Jiangsu Province (Grant number JZ-035).

## References

- [1] E. Nastri, M. D'Aniello, M. Zimbru et al., "Seismic response of steel moment resisting frames equipped with friction beam-to-column joints," *Soil Dynamics and Earthquake Engineering*, vol. 119, pp. 144–157, 2019.
- [2] V. Piluso, R. Montuori, E. Nastri, and A. Paciello, "Seismic response of MRF-CBF dual systems equipped with low damage friction connections," *Journal of Constructional Steel Research*, vol. 154, pp. 263–277, 2019.
- [3] H. Wang, Y. Feng, J. Wu, Q. Jiang, and X. Chong, "Damage concentration effect of multistory buckling-restrained braced frames," *Advances in Civil Engineering*, vol. 2019, Article ID 7164373, 15 pages, 2019.
- [4] E. Bojórquez, A. López-Barraza, A. Reyes-Salazar et al., "Improving the structural reliability of steel frames using posttensioned connections," *Advances in Civil Engineering*, vol. 2019, Article ID 8912390, 10 pages, 2019.
- [5] M. A. Bravo-Haro and A. Y. Elghazouli, "Permanent seismic drifts in steel moment frames," *Journal of Constructional Steel Research*, vol. 148, pp. 589–610, 2018.
- [6] D. Cardone and G. Gesualdi, "Influence of residual displacements on the design displacement of spherical friction-based isolation systems," *Soil Dynamics and Earthquake Engineering*, vol. 100, pp. 492–503, 2017.
- [7] J. Erochko, C. Christopoulos, R. Tremblay, and H.-J. Kim, "Shake table testing and numerical simulation of a self-centering energy dissipative braced frame," *Earthquake Engineering & Structural Dynamics*, vol. 42, no. 11, pp. 1617–1635, 2013.
- [8] N. Chancellor, M. Eatherton, D. Roke, and T. Akbaş, "Self-centering seismic lateral force resisting systems: high performance structures for the city of tomorrow," *Buildings*, vol. 4, no. 3, pp. 520–548, 2014.
- [9] C. Christopoulos, R. Tremblay, H.-J. Kim, and M. Lacerte, "Self-centering energy dissipative bracing system for the seismic resistance of structures: development and validation," *Journal of Structural Engineering*, vol. 134, no. 1, pp. 96–107, 2008.
- [10] J. Erochko, C. Christopoulos, and R. Tremblay, "Design and testing of an enhanced-elongation telescoping self-centering energy-dissipative brace," *Journal of Structural Engineering*, vol. 141, no. 6, Article ID 04014163, 2015.
- [11] C.-C. Chou and Y. C. Chen, "Development and seismic performance of steel dual-core self-centering braces," in *Proceedings of the 15th World Conference on Earthquake Engineering*, Lisbon, Portugal, September 2012.
- [12] C.-C. Chou, Y.-C. Chen, D.-H. Pham, and V.-M. Truong, "Steel braced frames with dual-core SCBs and sandwiched BRBs: mechanics, modeling and seismic demands," *Engineering Structures*, vol. 72, pp. 26–40, 2014.
- [13] C.-C. Chou, T.-H. Wu, A. R. O. Beato, P.-T. Chung, and Y.-C. Chen, "Seismic design and tests of a full-scale one-story one-bay steel frame with a dual-core self-centering brace," *Engineering Structures*, vol. 111, pp. 435–450, 2016.
- [14] A. Watanabe, Y. Hitomi, E. Saeki, A. Wada, and M. Fujimoto, "Properties of brace encased in buckling-restraining concrete and steel tube," in *Proceedings of the 9th World Conference on Earthquake Engineering*, Tokyo-Kyoto, Japan, August 1988.
- [15] K. L. Deng, P. Pan, X. G. Xu, P. Feng, and L. P. Ye, "Study of GFRP steel buckling restraint braces," *Journal of Composites for Construction*, vol. 19, no. 6, Article ID 04015009, 2015.
- [16] L. Liu and B. Wu, "Seismic response of steel frames with self-centering buckling-restrained braces," *Journal of Building Structures*, vol. 37, no. 4, pp. 93–101, 2016, in Chinese.

- [17] C.-C. Chou, W.-J. Tsai, and P.-T. Chung, "Development and validation tests of a dual-core self-centering sandwiched buckling-restrained brace (SC-SBRB) for seismic resistance," *Engineering Structures*, vol. 121, pp. 30–41, 2016.
- [18] Z. Zhou, X. T. He, J. Wu, C. L. Wang, and S. P. Meng, "Development of a novel self-centering buckling-restrained brace with BFRP composite tendons," *Steel and Composite Structures*, vol. 16, no. 5, pp. 491–506, 2014.
- [19] Z. Zhou, Q. Xie, X. C. Lei, X. T. He, and S. P. Meng, "Experimental investigation of the hysteretic performance of dual-tube self-centering buckling-restrained braces with composite tendons," *Journal of Composites for Construction*, vol. 19, no. 6, Article ID 04015011, 2015.
- [20] Q. Xie, Z. Zhou, J. Huang, D. P. Zhu, and S. P. Meng, "Finite-element analysis of dual-tube self-centering buckling-restrained braces with composite tendons," *Journal of Composites for Construction*, vol. 21, no. 3, Article ID 04016112, 2017.
- [21] L.-H. Xu, X.-W. Fan, and Z.-X. Li, "Development and experimental verification of a pre-pressed spring self-centering energy dissipation brace," *Engineering Structures*, vol. 127, pp. 49–61, 2016.
- [22] X. W. Fan and L. H. Xu, "Behaviors comparisons and prediction of pre-pressed spring self-centering energy dissipation braces," *International Journal of Structural Stability and Dynamics*, vol. 18, no. 8, Article ID 1840006, 2018.
- [23] L.-H. Xu, X.-S. Xie, and Z.-X. Li, "Development and experimental study of a self-centering variable damping energy dissipation brace," *Engineering Structures*, vol. 160, pp. 270–280, 2018.
- [24] D. J. Miller, L. A. Fahnestock, and M. R. Eatherton, "Development and experimental validation of a nickel-titanium shape memory alloy self-centering buckling-restrained brace," *Engineering Structures*, vol. 40, pp. 288–298, 2012.
- [25] A. Kari, M. Ghassemieh, and B. Badarloo, "Development and design of a new self-centering energy-dissipative brace for steel structures," *Journal of Intelligent Material Systems and Structures*, vol. 30, no. 6, pp. 924–938, 2019.
- [26] C. Qiu and S. Zhu, "Shake table test and numerical study of self-centering steel frame with SMA braces," *Earthquake Engineering & Structural Dynamics*, vol. 46, no. 1, pp. 117–137, 2017.
- [27] Y. Chen, W. Wang, and Y. Chen, "Full-scale shake table tests of the tension-only concentrically braced steel beam-through frame," *Journal of Constructional Steel Research*, vol. 148, pp. 611–626, 2018.
- [28] G. A. Papagiannopoulos, "On the seismic behaviour of tension-only concentrically braced steel structures," *Soil Dynamics and Earthquake Engineering*, vol. 115, pp. 27–35, 2018.
- [29] B. Tang, F. Zhang, Y. Wang, and F. Wang, "Effect of pre-stressed cable on pre-stressed mega-braced steel frame," *Structural Engineering and Mechanics*, vol. 59, no. 2, pp. 327–341, 2016.
- [30] European Committee for Standardization, *Eurocode 8: Design of Structures for Earthquake Resistance*, European Committee for Standardization, Brussels, Belgium, 2005.
- [31] ASCE 7-10, *Minimum Design Loads for Buildings and Other Structures*, American Society of Civil Engineers, Reston, VA, USA, 2010.
- [32] S. A. Mousavi and S. M. Zahrai, "Contribution of pre-slacked cable braces to dynamic stability of non-ductile frames; an analytical study," *Engineering Structures*, vol. 117, pp. 305–320, 2016.
- [33] S. A. Mousavi and S. M. Zahrai, "Slack free connections to improve seismic behavior of tension-only braces: an experimental and analytical study," *Engineering Structures*, vol. 136, pp. 54–67, 2017.
- [34] S. M. Zahrai, S. A. Mousavi, and M. Saatcioglu, "Analytical study on seismic behavior of proposed hybrid tension-only braced frames," *The Structural Design of Tall Special Buildings*, vol. 26, no. 3, p. e1310, 2017.
- [35] M. H. Mehrabi, Z. Ibrahim, S. S. Ghodsi, and M. Suhatri, "Seismic characteristics of x-cable braced frames bundled with a pre-compressed spring," *Soil Dynamics and Earthquake Engineering*, vol. 116, pp. 732–746, 2019.
- [36] P. Chi, J. Dong, Y. Peng, and J. Y. R. Liew, "Theoretical and numerical study on an innovative self-centering energy-dissipative tension-brace system," *Journal of Vibration and Shock*, vol. 35, no. 21, pp. 171–176, 2016, in Chinese.
- [37] P. Chi, T. Guo, Y. Peng, D. F. Cao, and J. Dong, "Development of a self-centering tension-only brace for seismic protection of frame structures," *Steel and Composite Structures*, vol. 26, no. 5, pp. 573–582, 2018.
- [38] SAP2000, *Structural Analysis Program, Version 17.3.0*, Computers and Structures, Inc., Berkeley, CA, USA, 2015.
- [39] FEMA 450, *NEHRP Recommended Provisions for Seismic Regulations for New Buildings and Other Structures: Part 1-Provisions and Part 2-Commentary*, Building Safety Seismic Council, Washington, DC, USA, 2003.
- [40] JGJ 99-2015, *Technical Specification for Steel Structure of Tall Building*, Ministry of Housing and Urban-Rural Development of China, Beijing, China, 2015.
- [41] GB 50011-2010, *Code for Seismic Design of Buildings*, Ministry of Housing and Urban-Rural Development of China, Beijing, China, 2010.
- [42] AISC 341-16, *Seismic Provisions for Structural Steel Buildings*, American Institute of Steel Construction, Chicago, IL, USA, 2016.
- [43] S. Kiggins and C.-M. Uang, "Reducing residual drift of buckling-restrained braced frames as a dual system," *Engineering Structures*, vol. 28, no. 11, pp. 1525–1532, 2006.

